Corrosion Science 148 (2019) 213–227

Contents lists available at ScienceDirect

Corrosion Science

journal homepage: www.elsevier.com/locate/corsci

An insight into PWR primary water SCC mechanisms by comparing surface and crack oxidation

Zhao Shen[a,*], Donghai Du[b,c,**], Lefu Zhang[b], Sergio Lozano-Perez[a]

[a] Department of Materials, University of Oxford, Parks Road, OX1 3PH, Oxford, UK
[b] School of Nuclear Science and Engineering, Shanghai Jiao Tong University, 800 Dongchuan Road, Shanghai, 200240, China
[c] University of Michigan, 2355 Bonisteel Blvd, Ann Arbor, MI, 48109, United States

ARTICLE INFO

Keywords:
Stainless steel
Surface oxidation
Crack tip oxidation
Stress corrosion cracking
Transmission electron microscopy

ABSTRACT

Oxidation and stress corrosion cracking (SCC) of 316L stainless steel were studied in simulated pressurized water reactor primary water. Surface, crack flank, and crack tip oxides were analyzed and compared by high-resolution characterization, including oxidation state mapping. All oxides were found to have a triplex structure, although of different dimensions and composition, revealing the effects of local water chemistry and applied stress. The higher oxidation rate at the crack tip could be explained due to the existence of a higher dislocation density, higher level of stress and cation unavailability from the environment. The implications to SCC mechanisms are discussed.

1. Introduction

Austenitic stainless steel (SS) type 316 L is widely used for critical components in pressurized water reactor (PWR) due to its combination of excellent mechanical property and high corrosion resistance in the high temperature aqueous environment. The oxide film developed on the surface of 316 SS in the PWR primary water environment plays an important role in protecting the material from further oxidation [1–10]. Similarly, oxidation at the crack tips develops into an intergranular oxidation zone (IOZ) ahead of the crack tip, which is crucial for understanding stress corrosion cracking (SCC) of SS components in a nuclear power plant [11–16]. Our recent work [13,17] suggests that higher intergranular oxidation rate could lead to higher SCC crack growth rate (CGR). In addition, the protectiveness of an oxide film is significantly affected by its microstructure [18,19]. According to the simulation work conducted by Vankeerberghen et al. [5], the water chemistry in the region close to the SCC crack tips is similar to that in the environment under PWR conditions. As a result, the mechanisms controlling the oxidation at outer surface and the crack tip might be similar and hence the microstructure of the oxides and the oxidation mechanisms at specimen outer surface and the crack tip.

Surface oxidation and crack tip oxidation have been extensively studied in literature [1–26], but inconsistent conclusions on the oxidation mechanisms were drawn due to the differences in experimental conditions and materials. To obtain the correlation between the oxides at surface and crack tip, it is of great importance to do a comparative study of the oxides developed on the surface and at the crack tip in the same material and under the same environment.

According to the work conducted in [1–3,18,19,21–26], the oxide film formed on SS in high temperature aqueous environment has duplex structure: a Cr-rich inner oxide layer and a Fe-rich outer oxide layer. Several mechanisms were proposed to rationalize this phenomenon. Stellwag [1] considers that the formation of the inner and outer oxide layer is determined by solid-state growth mechanism and metal dissolution-precipitation mechanism, respectively. Robertson [27] suggests that both layers are formed by the solid-state growth mechanism. Winkler et al. [28] assumes that both layers are formed by the metal dissolution-precipitation mechanism. Since there is still not a widely accepted explanation, more studies are needed to reveal the mechanisms controlling surface oxidation.

To accomplish these objectives, a 0.5 T (12.7 mm in thickness) compact tension (CT) and a plate specimen made of 20% cold worked 316 L SS were exposed to simulated PWR primary water for SCC and general corrosion testing. Dual beam focused ion beam (FIB) was used to prepare transmission electron microscopy (TEM) lamellae containing the SCC crack tip or the surface oxide. The TEM lamellae were analyzed by high-resolution analytical TEM (ATEM). The scope of this work includes:

1 Identifying the mechanisms controlling oxidation of 316 L SS

* Corresponding author.
** Corresponding author at: School of Nuclear Science and Engineering, Shanghai Jiao Tong University, 800 Dongchuan Road, Shanghai, 200240, China.
E-mail addresses: zhao.shen@materials.ox.ac.uk (Z. Shen), 0703ddh@sjtu.edu.cn (D. Du).

https://doi.org/10.1016/j.corsci.2018.12.020
Received 30 July 2018; Received in revised form 19 November 2018; Accepted 14 December 2018
Available online 25 December 2018

Table 1
Chemical composition of the material used in this study (wt%).

Material	C	Cr	Fe	Si	Mn	P	S	Mo	Ni
316 L SS	0.014	17.28	65.89	0.43	1.81	0.012	0.001	2.48	12.05

exposed to simulated PWR primary water.
2 Revealing the microstructure and chemistry of the crack flank and crack tip oxides, and comparing them with the surface oxide.
3 Discussing the underlying connections between oxidation and SCC mechanisms.

2. Experimental

2.1. Material and autoclave testing

The material used in this study was cold-forged 316 L SS with about 20% of plastic deformation. The grain size of the 316 L SS was around 100 μm and the chemical composition is shown in Table 1. The SCC and exposure test was conducted in simulated PWR primary water (hydrogenated water: 500 ppm B + 2 ppm Li + 30 cc/kg dissolved H_2) at 340 °C by the Joint Laboratory for Corrosion of Nuclear Power Materials at Shanghai Jiao Tong University (China). The autoclave and pipelines used in this study were made of 316 SS. A pre-cracked 0.5 T CT specimen prepared in the S-L orientation (according to ASTM E399) was used for SCC test. A piece of 316 L SS plate with dimensions of 20 mm wide, 30 mm long and 2 mm thick was exposed along with the CT specimen for 2000 h. Before the autoclave testing, the 316 L SS coupon was ground with SiC paper, followed by polishing with 1-μm diamond suspension. A mirror-finished surface was obtained after 15 min of final treatment with colloidal silica. The content of dissolved hydrogen was 30 cc/kg located at the equilibrium of Ni/NiO, which means it is difficult for the Ni to be oxidized during the SCC testing [20]. The CGR was measured to be around 6.21×10^{-8} mm/s, which was tested at a constant crack tip strength intensity factor (K) of 30 MPa $m^{1/2}$.

2.2. Methodology

2.2.1. Site-specific sample preparation with FIB

To study the oxide at the specific crack tip and surface, the FIB plan-view and cross-section sample preparation techniques were adopted, respectively. A single beam FEI FIB200 equipped with a static micromanipulator was used for trenching and in-situ lift-out. A dual beam Zeiss NVision 40 FIB-SEM was subsequently used for thinning the sample to a thickness less than 50 nm. Since FIB milling could introduce significant damage on the sample surface, a final low energy cleaning (5 kV, 250 pA) was performed on both sides of the thin foil after a conventional milling to minimize the damage. More details can be found in the reference [29].

2.2.2. ATEM analysis

TEM analysis was performed with a JEOL 2100 (LaB_6, operating voltage 200 kV) for TEM imaging and selected area diffraction. High-resolution analysis, including scanning TEM (STEM) and electron energy loss spectroscopy (EELS), was conducted with a JEOL ARM200 F (cold-field emission gun with a typical energy resolution of 0.4 eV) operating at 200 kV and equipped with a Quantum Gatan image filter (GIF) spectrometer. EELS spectra (low- and core-loss) were acquired correcting the spatial drift and recalibrated in energy using the zero-loss peak as a reference. Principal components analysis (for denoising) was performed using Hyperspy 1.3 (open source) software. The convergence and collection half-angles were 31 and 41 mrad, respectively, and a

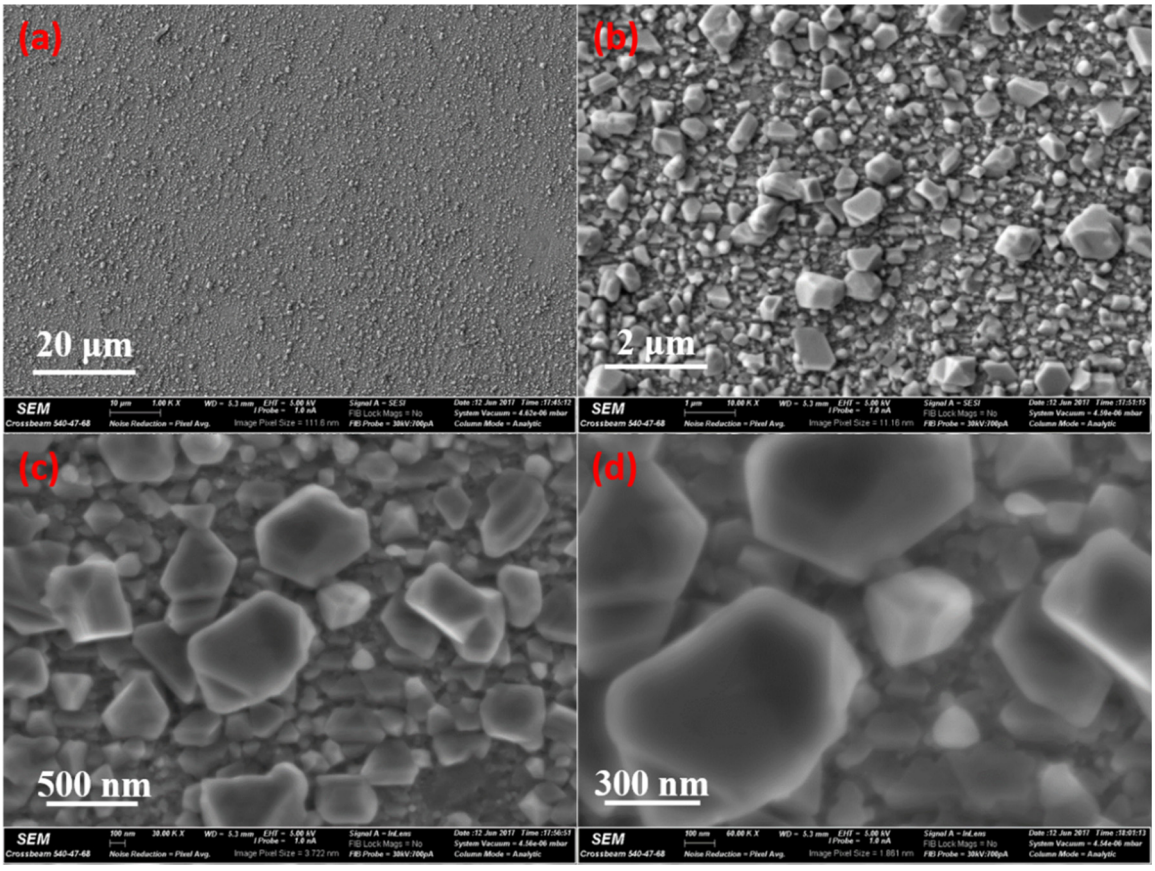

Fig. 1. Morphologies of the surface oxide formed on 316 L SS exposed to simulated PWR primary water at 340 °C for 2000 h.

dispersion of 0.25 eV/channel was used. EELS quantification was performed in Digital Micrograph by the background subtraction method. The relatively low thickness of all areas analyzed (˜50 nm) allowed for a reliable quantification without removing plural scattering. This was checked for regions of known composition (e.g. matrix). The relative errors in EELS quantification were dominated by uncertainties in theoretical cross-sections and can be assumed to be ˜10% relative for most measurements.

Experimental EELS spectra containing L edges of Cr, Fe and Ni were fitted in Hyperspy [30] as a linear combination of an inverse power law (background), a Hartree-Slater theoretical edge and two Gaussians (L_3 and L_2 white line peaks). The energy of the L_3 white line and the ratio between the areas of the L_3 and L_2 peaks were used to determine the oxidation state [31,32] of Cr and Fe. No conclusive results were obtained for the Ni edge, due to a combination of noise and minimal changes in fine-structure, so it was excluded from the analysis.

3. Results

3.1. Morphologies of the surface oxide

Fig. 1 shows the morphologies of the surface oxide on the coupon under different magnifications after exposure to the simulated PWR primary water at 340 °C for 2000 h. At low magnification, the morphology of the surface oxide was not clear and only tiny and discretely distributed particles can be discerned (see Fig. 1a). With increased magnification, these faceted particles proved to be polyhedral crystallites with sharp edges (see Fig. 1b). Their sizes range from less than 50 nm to 1 μm (see Fig. 1c). Although the distribution of big crystallites (relatively) was sparse, the distribution of the fine ones appeared to be compact (see Fig. 1d). Further observation reveals that the large crystallites appeared to distribute on top of the fine crystallites.

3.2. Cross-sectional morphologies of surface oxide

The cross-sectional morphology of the surface oxide was analyzed by TEM. Fig. 2a shows a thin layer of surface oxide on the matrix. Although the oxide film was continuous, the thickness was not uniform, ranging from 50 to 120 nm. Oxide particles were also observed, sitting on the top of the oxide film. The interface between the oxide film and the oxide particles was mostly straight and was considered to be the original sample surface, as highlighted by the red dashed line between the inner and the outer oxide layers. Oxide dissolution was observed when the original sample surface was used as a reference. At a higher magnification, the interface can be more easily observed and the oxide dissolution was further confirmed (see Fig. 2b). It appears that the oxide dissolution under the surface oxide particles was prevented (see Fig. 2a and b). With further increase of magnification, more details can be observed in the surface oxide film. As shown in Fig. 2c and d, both of the oxide films consist of a duplex structure. The inner oxide layer was composed of numerous nanocrystallites with the size of around 10 nm. Further observation reveals that the oxidation had penetrated into the matrix under the inner oxide layer. Since the oxide particles formed on the top surface of the oxide film were not continuous, they were not treated as a layer of oxide in the current study.

3.3. Crystallographic structures of surface oxide

To reveal the crystallographic structure of the surface oxide, atomic-resolution TEM imaging was conducted and fast Fourier transformation (FFT) was used to analyse the atomic-resolution images. Fig. 3a shows that the matrix was an austenitic phase. The nanocrystallites in the inner oxide layer were identified to be chromite-type spinel (see Fig. 3b). Interestingly, the outer part of the oxide next to the original surface appeared to be an amorphous continuous layer. FFT confirmed the presence of some crystalline periodicity (see Fig. 3c) and some degree of amorphization. Fig. 3d shows that the top surface oxide discrete particles were magnetite-type spinel. From now on, we will split the outer oxide layer in two regions: Outer oxide layer (continuous and partly amorphous) and outer oxide particles (discrete and mostly grown by precipitation from cations in the environment).

The structure of the surface oxides was also investigated using selective area electron diffraction (SAED), in order to better understand their epitaxial relationships. Fig. 4 depicts a cross-section of the surface oxide and the corresponding SAED patterns of the matrix and the surface oxides. Fig. 4b shows the SAED pattern obtained from the matrix. The selective area is marked as A (aperture size = 100 nm) in Fig. 4a. The matrix SAED pattern was indexed as austenite phase, as shown in Fig. 4b. Fig. 4d shows the SAED pattern obtained from the matrix and the inner layer oxide (region C in Fig. 4a), showing that the inner oxide was chromite-type spinel. In addition, the diffraction pattern of the oxide is coherent with the diffraction pattern of matrix in one direction, suggesting that there was an epitaxial relationship between the matrix and the inner layer oxide (see Fig. 4d). The aperture size used for region C was 100 nm. SAED was also conducted on region containing all surface oxides and matrix, marked as B (aperture size = 200 nm) in Fig. 4a. The SAED pattern proves that the surface oxides consisted of both chromite-type and magnetite-type spinel, as shown in Fig. 4c. As mentioned above, the inner layer oxide and the outer oxide particle were composed of chromite-type spinel and magnetite-type spinel, respectively. No epitaxial relationship was observed between the magnetite-type spinel and the matrix in Fig. 4c, suggesting that there was no crystallographic relationship between the outer oxide particles and the matrix. The SAED pattern in Fig. 4c was not as sharp as that in Fig. 4d, which could be due to the amorphous outer layer oxide described previously (see Fig. 3c).

3.4. Chemical composition of surface oxide

The morphology and chemical composition of the surface oxide films were examined via high angle annular dark field (HAADF) imaging and EELS analysis. Fig. 5a shows the HAADF image of the cross-section of the surface oxide formed on 316 L SS. Since the HAADF image is very sensitive to the atomic number of the material, it is easy to differentiate the oxide from the matrix through their different signal intensity. Surface oxidation was found to be continuous but the thickness was not uniform. The interface between the oxide and the matrix was not straight, showing a wavy shape. Further observation reveals that there were many black dots and channels in the matrix closed to the surface oxide, indicating that oxidation had developed into this region, as seen in Fig. 2. The difference in contrast was not enough to appreciate the duplex nature of the oxide film in the HAADF images.

EELS mapping was also conducted and the results are shown in Fig. 5b and c. Fig. 5b shows the signal intensity maps (net elemental counts), in which the brighter regions contain a higher net content of elements. The O-map in Fig. 4b reveals that discrete oxidation might have occurred into the metal beyond the matrix-inner oxide interface, in the form of very fine entangled filaments, likely to be individual oxidized dislocations, which do not seem directly connected to the inner oxide. We will refer to this new layer as “penetrative oxidation layer”. EELS analysis reveals that Cr was enriched while Fe was depleted in the O-rich region (see the Cr-map and Fe-map in Fig. 5b). The Ni-map shows that the Ni was depleted in the O-rich region but enriched in the region surrounding the oxide. Atomic-resolution imaging was also conducted, revealing that the oxide in the penetrative oxidation layer was mainly composed of Cr_2O_3 and $FeCr_2O_4$ and the oxides were epitaxial with the surrounding matrix (not shown). In the Cr-map, the original surface of the sample can be identified due to the different signal intensity, which is highlighted by a blue dashed line. Oxide dissolution can be observed when the position of the original surface was used as a reference, as marked by a green dashed circle. Further observation reveals that there was a Cr-rich layer on the top of the

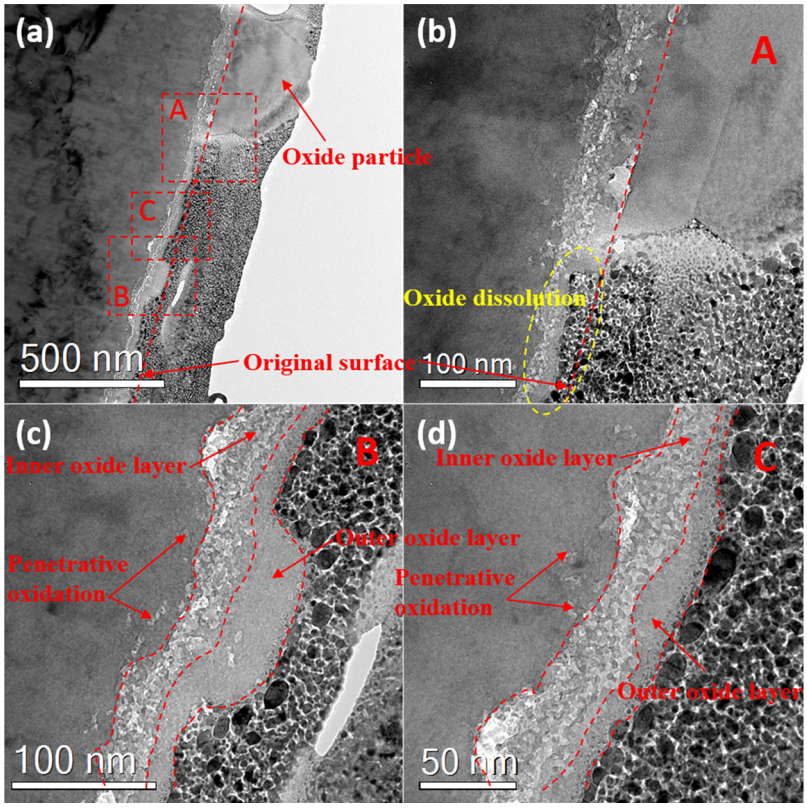

Fig. 2. (a) TEM images showing the cross-section of the surface oxide; (b) a magnified view of the rectangular area A in (a); (c) a magnified view of the rectangular area B in (a); (c) a magnified view of the rectangular area C in (a).

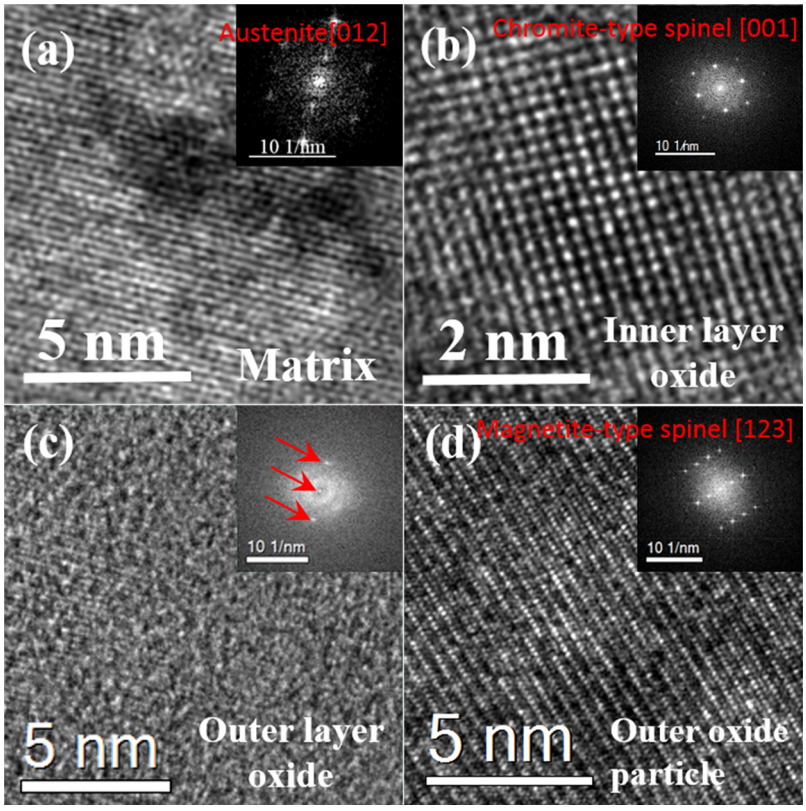

Fig. 3. Atomic-resolution images of the surface oxide formed on 316 L SS exposed to simulated PWR primary water: (a) atomic-resolution TEM image showing the matrix in the zone axis of [012]; (b) atomic-resolution TEM image showing the inner layer chromite-type spinel oxide in the zone axis of [001]; (c) atomic-resolution TEM image showing that outer layer oxide was amorphous; (d) atomic-resolution TEM image showing that the outer oxide particle was magnetite-type spinel in the zone axis of [123].

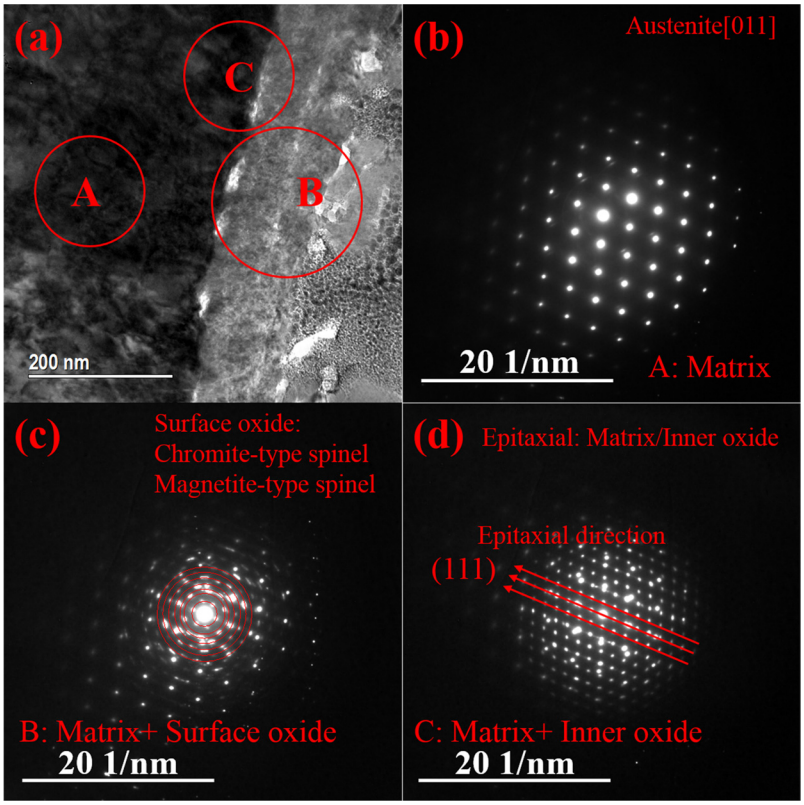

Fig. 4. (a) TEM micrograph; (b) SAED pattern obtained from A- matrix; (c) SAED pattern obtained from C- matrix and surface oxide; (d) SAED pattern obtained from D-matrix and inner oxide layer.

penetrative oxidation layer, corresponding to the position of inner oxide layer. The structure of this layer was continuous but the thickness was not uniform, ranging from 30 to 100 nm. The Fe-map and Ni-map show that Fe and Ni were depleted in this layer. On the top of the inner oxide layer, lies the outer oxide layer, which was enriched in Fe and Ni but depleted in Cr, as shown in Fig. 5b. Several outer oxide particles were observed on the original surface and the bigger ones were observed to growth on the top of the small ones (see the Fe-map in Fig. 5b). The chemical composition of the oxide particles was similar to the outer oxide layer. Fig. 5c shows the relative chemical composition maps (concentration in atomic percentage) obtained from EELS mapping. Compared with the signal intensity maps, the relative composition maps were similar except for the distribution of O in the surface oxide film. The relative composition O-map shows that the relative content of O in the whole surface oxide film (excluding the penetrative oxidation layer) was similar although the signal density of O was not uniform (see the O-map in Fig. 5b). To study the elemental distribution across the surface oxide film, a quantitative line-scan was conducted. The line-scan position is indicated in the Cr-map of Fig. 5c and the results are shown in Fig. 5d. Due to the different chemical composition, it is easy to distinguish the different layers of oxide from each other. As shown in Fig. 5d, I–IV represent the outer oxide particles, outer oxide layer, inner oxide layer, and penetrative oxidation layer, respectively. A qualitative EELS line-scan, showing the integrated EELS signal, was also extracted, as shown in Fig. 5e, since it is more useful to understand elemental diffusion. In this line profile, it can be seen that the signal intensity of Cr in the inner oxide layer was even higher than in the unaffected matrix, indicating that Cr from the other regions has diffused into the inner oxide layer. Since regions II and III nearly have the same length, the increased Cr in the inner oxide layer can be described by the area of S_2. Compared with the unaffected matrix, the outer oxide layer was depleted in Cr and the decreased Cr can be described by the area of S_1. The area of S_1 was around two times greater than S_2.

According to the results described above, the surface oxide film mainly consisted of outer oxide particles (I), an outer oxide layer (II), an inner oxide layer (III), and a penetrative oxidation layer (IV), as shown in Fig. 5d. Their chemistry and microstructure are summarized in Table 2.

3.5. Morphologies and chemical composition of crack flank oxide

Fig. 6a shows the HAADF image of a crack prepared from 316 L SS exposed to simulated PWR primary water at 340 °C. The crack flank was prepared from a region around 1 μm away from a potentially active crack tip. Crack flanks were oxidized and the crack opening was filled with oxide (similar to the oxide particles on the surface oxide film). The oxidation in the crack flank reached 50–100 nm. EELS mapping was conducted to reveal the chemical composition of the oxides. Fig. 6b shows the signal intensity maps. The oxide in the crack opening was mainly composed of Fe and O. The original surface of the crack flanks can be identified in the Cr-map, which were marked by a green dashed line, as shown in the Cr-map of Fig. 6b. Further observation reveals that the oxide under the crack flank surface can be divided into two layers: an inner oxide layer and a penetrative oxidation layer. The inner oxide layer was enriched in Cr while depleted in Fe and Ni. The penetrative oxidation layer was very similar to that in the surface oxide film (see Fig. 5), with Cr-rich oxides surrounded by Ni, as shown in Fig. 6b. The relative composition maps shown in Fig. 6c were similar to the signal intensity map in Fig. 6b, except that the relative O content appeared to be higher in the inner oxide layer than the oxide in the crack opening. To understand the chemical composition in the crack flank oxide, a quantitative EELS line-scan was conducted. As shown in Fig. 6d, I, III, and IV represent the crack flank outer oxide particles, inner oxide layer, and penetrative oxidation layer, respectively. The crack flank outer oxide particles and inner layer oxide are compatible with Fe_3O_4 and $FeCr_2O_4$, respectively, according to the diffraction analysis and their

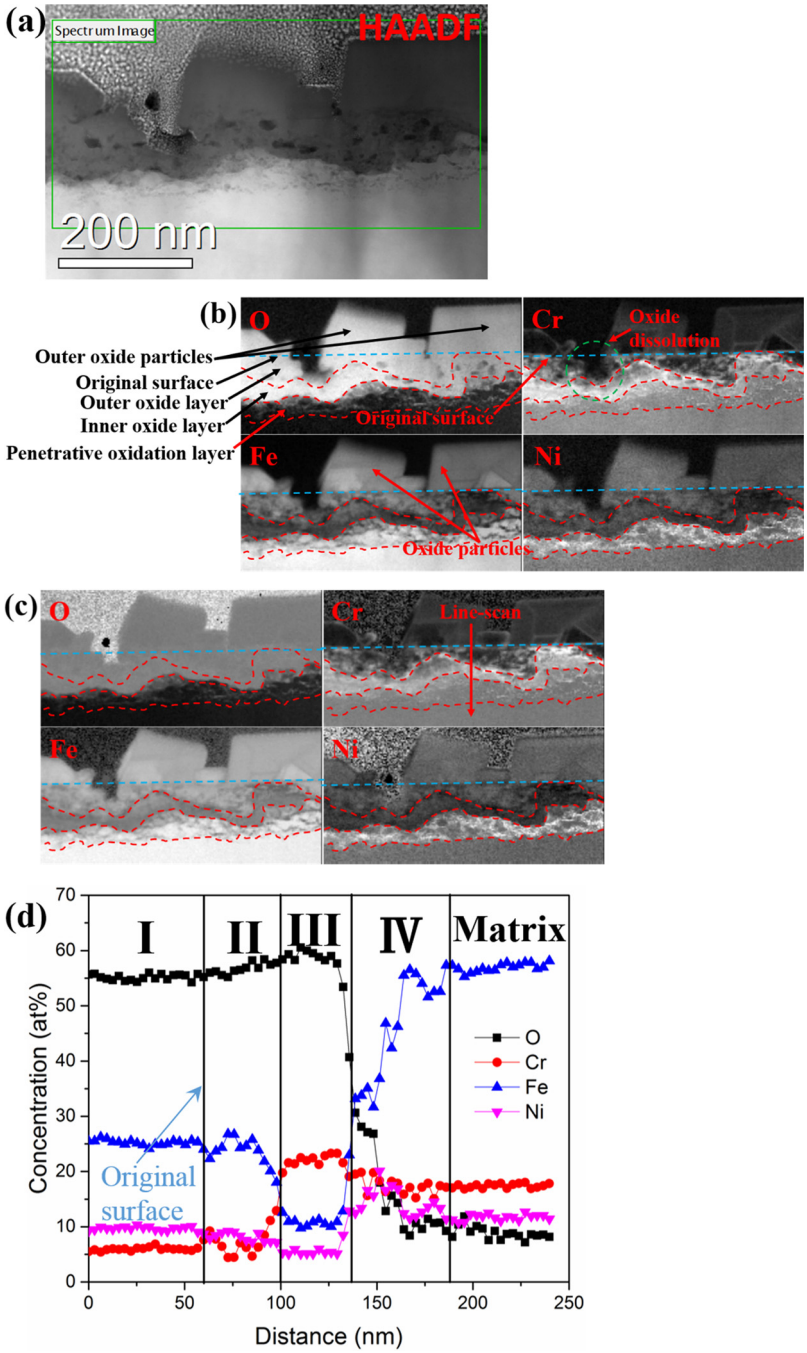

Fig. 5. Morphology and chemistry of the cross-section of the surface oxide formed on 316 L SS. (a) HAADF image; (b) EELS elemental O K edge and Cr/Fe/Ni L edge maps (signal counts); (c) EELS elemental O K edge and Cr/Fe/Ni L edge maps (relative composition); (d) EELS relative composition line profiles across the surface oxide; (e) EELS signal counts line profiles across the surface oxide.

Table 2
Summary of the chemical content, phases, and epitaxial relationship with matrix of the different oxide layers of surface oxide.

Surface oxide	Chemical content (at%)				Phases	Epitaxial with matrix
	O	Cr	Fe	Ni		
I	48~52	5~7	24~28	7~11	$(Fe,Cr,Ni)_3O_4$	No
II	54~58	3~15	15~28	5~10	Amorphous	No
III	57~62	18~25	10~15	3~5	$FeCr_2O_4$	Yes
IV	7~35	15~20	30~60	10~20	Cr_2O_3/ $FeCr_2O_4$	Yes

atomic ratios. SAED pattern show that the inner oxide layer was epitaxial with the matrix and no amorphous outer oxide (II in Fig. 5) was observed in the crack flank oxides. Since the exact composition of the tiny oxides in the penetrative oxidation layer cannot be easily extracted from the integrated thickness data, higher resolution analysis is needed.

To better observe the penetrative oxidation layer, a higher resolution EELS map was acquired and the results are shown in Fig. 7. Fig. 7a shows the HAADF image of an oxidized crack flank. Many discretely distributed black dots were observed in the matrix just beneath the inner oxide layer, indicating that oxidation had developed into this region. The EELS relative composition maps show that the black dots mainly consisted of O, Cr, and Fe and the Ni appeared to be “expelled” to the surrounding environment forming many Ni-rich channels (see

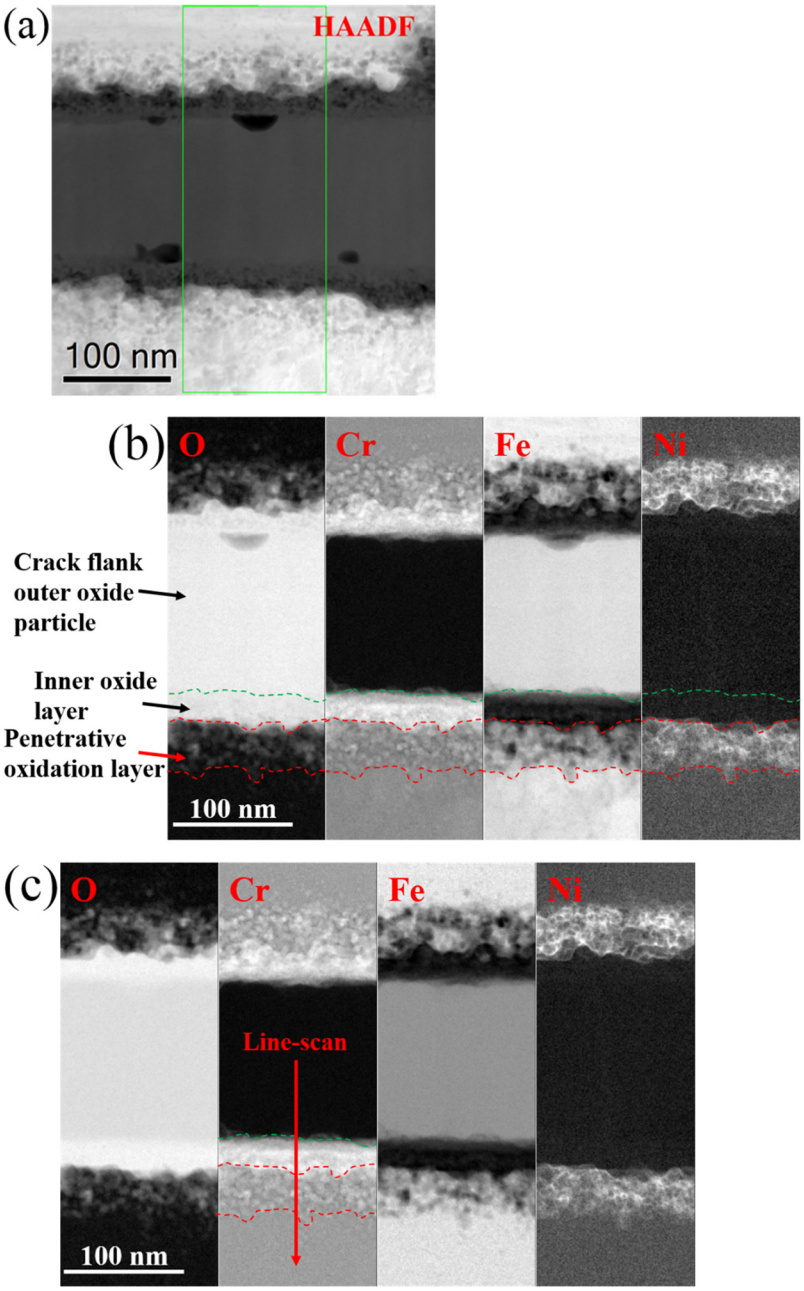

Fig. 6. Crack flank oxidation of 316 L SS exposed to simulated PWR primary water at 340 °C: (a) HAADF image; (b) EELS elemental O K edge and Cr/Fe/Ni L edge maps (signal intensity); (c) EELS elemental O K edge and Cr/Fe/Ni L edge maps (relative composition); (d) EELS composition line profiles across the crack flank.

Fig. 7b). EELS spectra extracted from the black dot (point A) and the matrix (point B) are given in the Fig. 7c and d, respectively. Compared with the spectrum from the matrix, the Ni peak disappeared in the black dot, indicating that there was no Ni in the black dot and the oxide in this layer might be $FeCr_2O_4$. Cr_2O_3 might also exist in this layer, since there were some regions only enriched in O and Cr, and depleted in Fe. To further confirm this hypothesis, atomic-resolution imaging was conducted, revealing that the oxides in this layer were mainly composed of $FeCr_2O_4$ and Cr_2O_3 and they were epitaxial with the surrounding matrix (not shown).

According to the results described above, the crack flank oxide film mainly consisted of outer oxide particles (I), an inner oxide layer (III), and a penetrative oxidation layer (IV), as shown in Fig. 6d. The chemistry and microstructure of the different layers are summarized in Table 3.

3.6. Morphologies and chemical composition of crack tip oxide

All crack tips observed in the CT specimen were intergranular and three potentially active SCC crack tips were prepared by FIB and examined by HAADF imaging and EELS analysis. One typical result is shown in Fig. 8. Fig. 8a shows the HAADF image of a crack tip specimen and the location of the crack tip is marked by a black arrow. In this study, crack tips are defined as the last portion of the GB (oxidized or not) directly exposed to the environment. To identify the position of crack tips in the TEM samples, HAADF imaging combined with Fresnel contrast in TEM mode were used [13]. Intergranular oxidation was observed in the region ahead of the crack tip. The length of this region was around 300 nm. The distribution of oxides was not uniform, with discretely distributed black spots that might be interconnected in 3D, but not within the thickness of the TEM sample. Fig. 8b shows the EELS signal intensity maps. The grain boundary ahead of the crack tip was

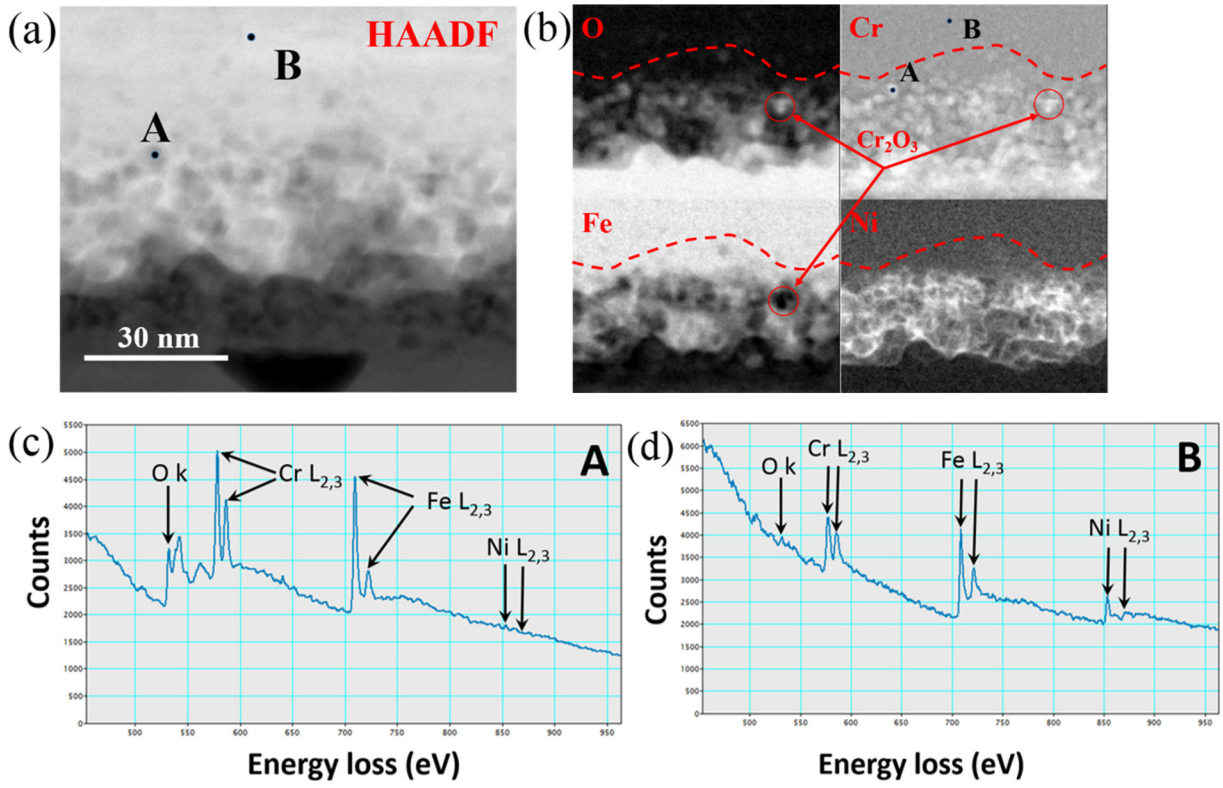

Fig. 7. (a) Magnified view of the crack flank oxidation of 316 L SS; (b) EELS elemental O K edge and Cr/Fe/Ni L edge maps (relative composition); (c) EELS spectrum obtained from point A; (d) EELS spectrum obtained from point B.

Table 3
Summary of the chemical content, phases, and epitaxial relationship with matrix of the different oxide layers of crack flank oxide.

Crack flank oxide	Chemical content (at%)				Phases	Epitaxial with matrix
	O	Cr	Fe	Ni		
I	53˜56	0	40˜43	0	Fe_3O_4	No
III	54˜58	20˜30	12˜25	2˜5	$FeCr_2O_4$	Yes
IV	5˜25	15˜22	35˜60	10˜20	Cr_2O_3/ $FeCr_2O_4$	Yes

enriched in Ni while depleted in Cr and Fe. The length of the Ni-rich zone was around 400 nm. Intergranular oxidation was confirmed to occur and the distribution of O appears to be discontinuous (see the O-map in Fig. 8b). Cr was significantly enriched in the O-rich region while Fe and Ni were depleted. Atomic-resolution imaging was conducted in the Region A (see Fig. 8a) and the oxide was revealed to be Cr_2O_3 (see Fig. 8d). Discretely distributed Cr_2O_3 precipitates embedded in spinel were also observed by Meisnar et al. [11] using APT in the region ahead of SCC crack tips. Further observation reveals that Cr was also enriched just ahead of the crack tip, although with a content not as high as that in the big black dots (i.e. Region A in Fig. 8a), being identified as $FeCr_2O_4$ (see Fig. 8e). The length of this region was around 40 nm. All the oxides observed ahead of crack tips were epitaxial with the matrix and amorphous structure was not observed in this region. In addition, in the open crack region behind the crack tip, crack flank oxidation also occurred and the penetrative oxidation was observed to develop into both of the crack flanks, which is similar to what was observed in Fig. 6. Penetrative oxidation was also observed to develop from the uncracked oxidized grain boundary ahead of the crack tip into the grains, although the extent was much lower than in the open crack region. The EELS relative composition maps shown in Fig. 8c were similar to the signal intensity maps. To quantitatively show the chemical composition across the oxidized grain boundary ahead of the crack tip, an EELS line-scan was conducted. The location of the line-scan is marked in the O-map of Fig. 8c. Fig. 8f shows that the intergranular oxidation propagated along the interface between the matrix and the Ni-rich zone. It is necessary to point out that the length of the Ni-rich zone (˜ 400 nm) was longer than the IOZ (˜300 nm) ahead of the crack tip, as shown in the supplementary data (see Fig. S1). An IOZ has been often associated with the formation of a Ni-rich region in Ni-based alloys [11–16] and the Ni-rich region has been proved to be the result of grain boundary migration [12,13,16,33–38]. The Ni-rich region occurred in this study was also revealed to be the result of grain boundary migration (via dynamically tilting the TEM sample under TEM) and the oxidation was observed to develop along the migrated grain boundary and not the original grain boundary (see Fig. 8f), which is consistent with the results in [12,13,16,33–38].

According to the results described above, the intergranular oxide developed ahead of crack tips consisted of a continuous Cr-rich oxide (III) similar to the inner oxide layer in the previous regions and discrete higher Cr oxides (IV) similar to the penetrative oxidation layer also shown before, as shown in Fig. 8b. The results obtained above are summarized in Table 4.

3.7. Oxidation state results

To better understand the type of oxides formed in each layer and what type of divalent or trivalent cations were preferred, oxidation state EELS maps were calculated for the three regions described in the previous sections. The maps revealed discrete oxidation states for Fe (0, 2+ and 3+) and Cr (0 and 3+), in agreement with the observed phases. The energy loss of the Fe and Cr L_3 lines was used to qualitatively map their oxidation states, as shown in Fig. 9. The values obtained for the energy loss of the L_3 line and the ratio between L_3/L_2 in the various oxidation states are shown in Table 5 and were extracted from the spectra shown in Fig. 10. Cr only appears as a trivalent (3+)

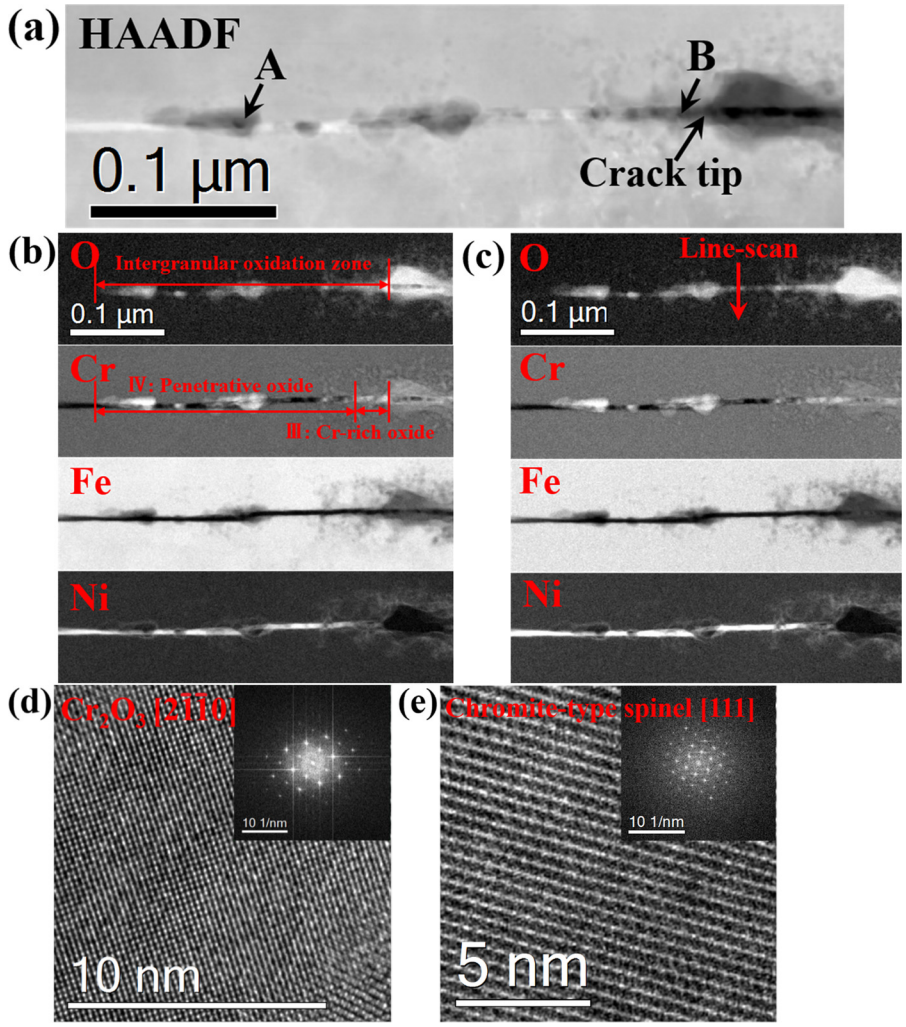

Fig. 8. Crack tip oxidation of 316 L SS exposed to simulated PWR primary water at 340 °C: (a) HAADF image; (b) EELS elemental O K edge and Cr/Fe/Ni L edge maps (signal intensity); (c) EELS elemental O K edge and Cr/Fe/Ni L edge maps (relative composition); (d) atomic-resolution TEM image showing that the oxide in the Region A was Cr_2O_3 in the zone axis of [2110]; (e) atomic-resolution TEM image showing that the oxide in the Region B is chromite-type spinel in the zone axis of [111]; (f) EELS composition line profiles across the oxidized grain boundary.

Table 4
Summary of the chemical content, phases, and epitaxial relationship with matrix of the different oxide layers of crack flank oxide film.

Crack tip oxide	Chemical content (at%)				Phases	Epitaxial with matrix
	O	Cr	Fe	Ni		
III	57˜62	19˜27	8˜15	3˜5	$FeCr_2O_4$	Yes
IV	54˜58	30˜40	2˜5	2˜5	Cr_2O_3	Yes

cation in this study when oxidized, which is compatible with the existence of chromia (Cr_2O_3) and chromite ($FeCr_2O_4$). The spinel have $M1M2_2O_4$ structure, where M1 is a divalent cation (2+) and M2 a trivalent one (3+). Fe is mostly incorporated to chromite as the divalent cation (2+) and to magentite as both divalent (33%) and trivalent (66%). Penetrative discrete oxides seem to mostly contain chromia, with some overlapping from unoxidized Fe (oxidation state 0), coming from the surrounding matrix due to the integration of the signal over the thickness of the TEM sample. Inner oxides spectra are compatible with chromia and chromite phases. The outer oxide shows a joint contribution from Fe 2+ and 3+, which matchs the magnetite phase ($FeFe_2O_4$). A higher 3+ contribution is observed in the outer part of the inner oxide in most regions and particularly in the amorphous outer oxide from the surface sample.

4. Discussion

The surface oxides formed on 316 L SS after exposure to simulated PWR primary water at 340 °C for 2000 h have been examined in detail at several locations. The inner oxide films can be divided into two regions: a continuous inner oxide layer and a discontinuous penetrative oxidation layer. The outer oxide can exhibit up to two layers: a discontinuous layer of oxide particles and a continuous amorphous outer oxide layer. These layers, as well as their roles and mechanisms of formation will be discussed next.

4.1. Oxide layers

4.1.1. Penetrative oxidation layer

The penetrative oxidation layer can be considered as part of the inner oxide layer, although in its early stages. It is the closest to the metal matrix and appears to follow defects in the microstructure, mostly dislocations. It is formed by discrete oxide nodules that follow the dislocation lines. Their discrete, unconnected nature was confirmed through tilt series (not shown) and by atom-probe tomography in previous works from the group [11,24]. It has been observed in three

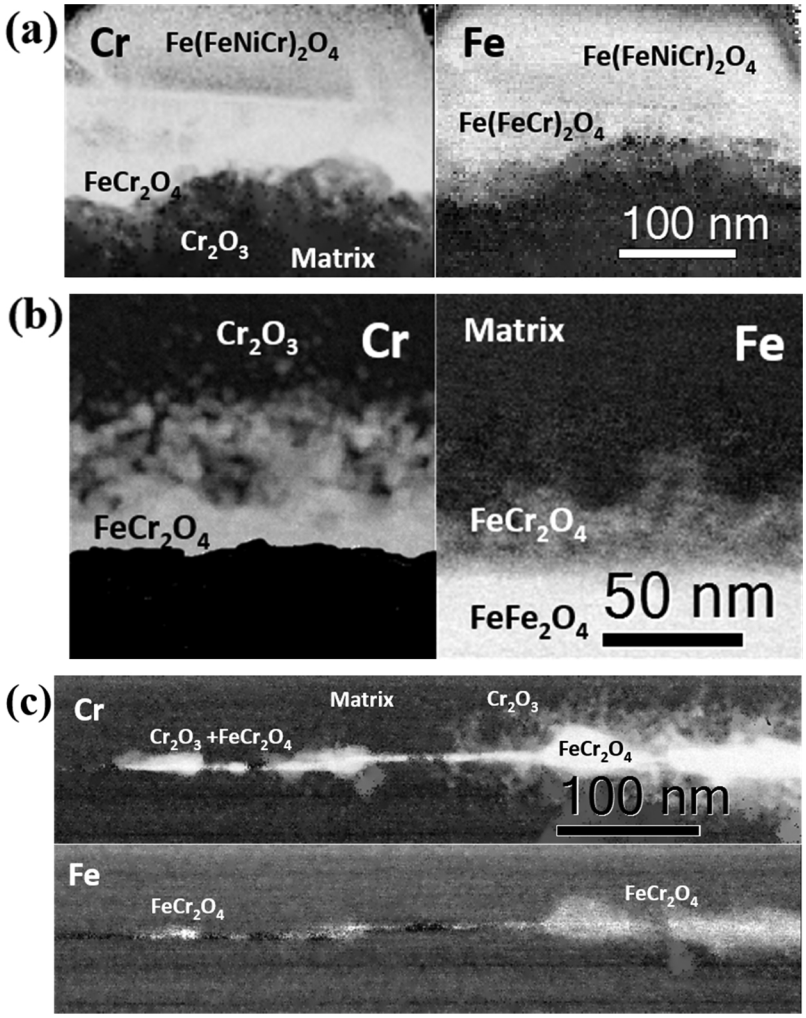

Fig. 9. L_3 energy-loss maps (brighter means higher energy-loss, correlated with a higher oxidation state) showing the different oxidation states. Cr is 3+ in Cr_2O_3 and $FeCr_2O_4$. Fe is 2+ in $FeCr_2O_4$ and 2+ and 3+ in $FeFe_2O_4$. (a) Surface oxide; (b) crack flank oxide; (c) crack tip oxide.

Table 5
Experimental values obtained for the energy of the L_3 line peak (± 0.1 eV) and the ratio between L_3/L_2 (± 0.04) for Fe and Cr L edges.

Elements	Metallic (0)		Oxidized (2+)		Oxidized (3+)	
	L_3 (eV)	L_3/L_2	L_3 (eV)	L_3/L_2	L_3 (eV)	L_3/L_2
Cr	576.2	1.47	–	–	577.3	1.52
Fe	707.8	2.0	708.5	4.0	709.0	5.1

regions, being enriched in Cr while depleted in Fe and Ni. Although the nodules were smaller than the sample thickness and quantitative results were affected by surrounding matrix, oxidation state mapping and diffraction confirmed the existence of chromia as the most likely oxide forming in this region. As can be seen in the maps in Fig. 9, the areas where the penetrative oxide is formed only shows oxidized Cr, while Fe remains metallic. This suggests that chromia initially forms to be later converted to chromite as the oxidation progresses. The depletion of Fe in the penetrative oxidation layer might be caused by the outward diffusion of Fe into the solution. The enriched Cr seemed to come from the matrix surrounding it because Cr-depletion was observed in the matrix. To support this hypothesis, the normalized signal densities of Cr, Fe, and Ni in the penetrative oxidation layer were compared to the normalized signal densities of Cr, Fe, and Ni in the unaffected matrix, respectively. The results show that the normalized signal density of Cr in the penetrative oxidation layer was similar to (only ˜5% lower) that in the unaffected matrix, confirming that the Cr in the penetrative oxidation layer was only locally redistributed by the selective oxidation and only around 5% of Cr diffused out into the inner oxide layer. The normalized signal density of Fe in the penetrative oxidation layer was measured to be around 20% lower than in the unaffected matrix, suggesting that around 20% of Fe diffused out during the exposure. Interestingly, the normalized signal density of Ni in the penetrative oxidation layer was around 25% higher than that in the unaffected matrix. To answer the question of where the increased Ni was diffusing from, there are two possible explanations: one being from the matrix under the penetrative oxidation layer and the other one from the inner oxide layer above. Since no Ni-depletion was observed in the matrix under the penetrative oxidation layer, the only possible explanation was that the increased Ni was from the region now occupied by the inner oxide layer.

Actually, the redistribution of Fe, Cr, and Ni in the penetrative oxidation layer could be related to their different diffusion rates, solubility in high temperature water and different affinities with oxygen. As the diffusion rate of Fe in the oxide is faster than that of Cr and Ni [27,39], the concentration gradient of Fe at the interface of matrix and the inner oxide layer will drive Fe to diffuse from the penetrative oxidation layer to the solution through the oxide film. Meanwhile, the inward diffusion of O will firstly react with Cr due to its high oxygen affinity. The Ni will be “expelled” to the surrounding matrix due to its low diffusion rate and low oxygen affinity under the water chemistry used in the current study [13,20,40]. In another words, the oxidation

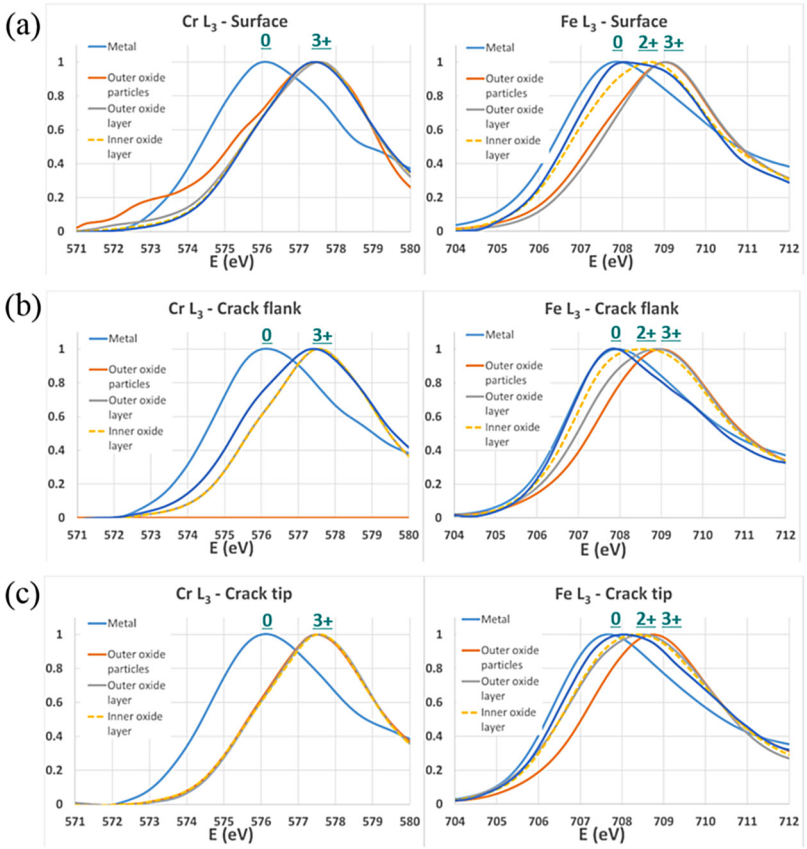

Fig. 10. EELS spectra showing the a comparison of the Cr (left column) and Fe (right column) L_3 edges depending on the location within the oxide for surface (a), crack flank (b) and crack tip (c) oxides.

observed appears to be selective (this is also known as dealloying in literature). The selective oxidation occurred in the inner oxide layer will also expel part of the Ni into the penetrative oxidation layer, resulting in the increase of Ni in the penetrative oxidation layer. The selective oxidation-induced Ni expulsion was also observed by Langelier et al. [40] using 3D atom probe tomography (APT) and by Sennour et al. [14] using atomic-resolution TEM.

Although the surface oxidation of SS in high temperature aqueous environments has been studied extensively, the penetrative oxidation layer was rarely reported [1–10,14–19,21]. A potential reason could be the lower resolution of the characterization techniques used in those studies. In the current study, the combination of a Cs-corrected STEM and a cold-field gun provided high lateral resolution imaging and high energy resolution chemical analysis. In comparison, the main analytical technique used in the literature [1–10,14–19,21] was EDX, which was not efficient in the detection of light elements such as O or lacked resolution. This is why Ni enrichment was always observed at the matrix/oxide film interface while O was not detected in this region. Another point to mention is that the Ni-rich zone was believed to be formed only due to the outward diffusion of other metallic elements from this region [1–10,14–19,21]. However, according to the EELS signal density maps shown above (see Fig. 5b), the inward expulsion of Ni from the inner oxide layer also contributed the localized Ni enrichment, as discussed above. The observation of a Ni-rich region around the penetrative oxidation layer might be helpful in understanding the SCC since a Ni-rich region was always observed ahead of the SCC crack tip and it was believed to have a significant effect on crack growth [11–13,29]. More details will be discussed later.

According to the results obtained in this study, we can conclude that in the early stage of surface oxidation, Cr was firstly oxidized by the inward diffusion of O through the fast-diffusion channels (possibility dislocation channels), while Ni was “expelled” to the surrounding matrix and Fe diffused from the matrix to the solution. This is consistent with the results reported by Kuang et al. [17], in which 304 SS was studied after exposed for 26 h in high-temperature water.

4.1.2. Inner oxide layer

Once the specimen was exposed for a longer time, the chromia in the penetrative oxidation layer will transform into chromite, forming the inner oxide layer. This has been confirmed by oxidation state mapping. It has been observed in the three regions. In Fig. 9, it can be seen how both the Fe and the Cr appeared oxidized in the inner oxide area (all samples). The energy loss of the L_3 peak in Fig. 10, suggests Cr is oxidized to 3+ and Fe mostly to 2 + . Interestingly, the closer the region it is to the open environment (e.g. sample surface), the higher the Fe 3+ content, particularly on the outer part of the inner oxide (described as the amorphous outer oxide layer for the surface sample). This suggests that the environment can provide with 3+ cations to the oxide, with its availability decreasing as one travels deeper into the crack.

Compared with the penetrative oxidation layer, the content of O in the inner oxide layer was higher although this could be an artefact caused by the size of the oxides in the penetrative oxidation layer being smaller than the thickness of the TEM foil. This hypothesis can be supported by the results reported by Lozano-Perez et al. [9,24] via atom probe tomography (APT). Compared with the unaffected matrix, the normalized signal density of Ni in the inner oxide layer was around 55% lower and Fe was around 75% lower while Cr was around 35% higher. The decrease of Fe was the result of outward diffusion due to its fast element diffusion rate [22,26], while the loss of Ni was the result of selective oxidation expelling Ni into the penetrative oxidation layer and the dissolution of Ni into the solution. Cr enrichment was frequently

reported in the inner oxide layer and it was attributed to the outward diffusion of Cr from the matrix to inner oxide layer [2,3,14,16,21]. However, the normalized signal density of Cr in the penetrative oxidation layer and the inner oxide layer was still around 30% higher than that in the unaffected matrix. If the increased Cr in the inner oxide layer only originated from the penetrative oxidation layer (e.g. from the volume now mostly occupied by Ni), the normalized signal density of Cr in the penetrative oxidation layer and the inner oxide layer should be similar to the unaffected matrix. As a result, the only possible explanation is that some of the extra Cr in the inner oxide layer comes through the outer oxide layer from the solution. However, the driving force for the inward diffusion of Cr from the solution into the inner oxide layer is still unclear at this stage and further study is needed.

According to the SADP patterns shown in Fig. 4, the inner oxide layer grew epitaxially with the matrix, indicating that its formation was dominated by the solid-state growth mechanism. Combining the SADP patterns in Fig. 4 and the chemical composition in Fig. 5, the Cr-rich chromite-type spinel oxide formed in the inner oxide layer can be formulated as $FeCr_2O_4$, which is consistent with the literature [1–10,14,16,17,19,22].

4.1.3. Outer oxide layer

Only the surface sample directly exposed to the environment exhibited an amorphous outer oxide layer as described in Sections 3.2 and 3.3. It is suggested that in this region, with increasing exposure times, a part of the inner oxide layer will turn into outer oxide layer (see Fig. 5). Although this layer had amorphous structure, the oxidation state maps reveal that there were higher proportion of Fe 3+ (see Figs. 9 and 10).

Compared with the unaffected matrix, its chemical composition for Fe, Ni, and Cr were around 45%, 40%, and 56% lower in the outer oxide layer, respectively. However, compared with the chemical composition in the inner oxide layer, Fe was around 120% higher in the outer oxide layer while Cr was 130% lower. The signal density of Ni in the outer oxide layer was around 15% higher than in the inner oxide layer. Since the formation of the outer oxide layer was the result of longer exposure of the inner oxide layer, the alteration of chemical composition in the outer oxide layer can be explained by the different diffusion rates of Cr, Fe, and Ni through the Cr-rich spinel oxide. According to Stellwag [1], the diffusion rate of Cr in the Cr-rich spinel oxide was much lower than Fe and Ni. When the Cr-rich inner oxide layer was exposed to the PWR water for longer time, Cr, Fe, and Ni in this layer would partially dissolve into the high-temperature solution. At the same time, the Cr, Fe, and Ni in the penetrative oxidation layer would diffuse into the inner oxide layer to supplement the loss of metallic elements. However, since the outward diffusion rate of Cr was much lower than Fe and Ni, the supply of Cr was lower than the loss. As a result, the outmost part of the inner oxide layer would end up depleted in Cr, creating the outer oxide layer (see Fig. 5). Since Cr in the oxide is critical in protecting material from further oxidation [1–10,18,19,21–26], the decrease of Cr in the outer oxide layer will enable more outward diffusion of metallic elements and inward diffusion of O, resulting in faster oxidation. In addition, Cr was reported to be crucial in stabilizing the spinel oxide in the PWR primary water environment [1]. The decrease of Cr in the outer oxide layer will accelerate the dissolution of the outer layer oxide (see Figs. 2 and 5). According to the atomic-resolution image shown in Fig. 3c, the structure of the outer layer oxide appeared to be amorphous. Thermodynamically, an amorphous phase is generally believed to be unstable, which might be able to explain why the oxide dissolution occurred in the outer oxide layer.

It is necessary to point out that although the duplex structure of the surface oxide formed on SS has been often reported in the past [1–10,18,19,21–26], the description of the outer oxide layer in the current study is different from that in literature, where it is closer to what we now refer to as the “outer oxide particles”. Traditionally, the layers were differentiated by composition, with the outer oxide layer Fe-rich and the inner one Cr-rich. However, in the current study, the outer surface oxide particles were not treated as a layer of oxide, since they are not continuous and are mostly formed by precipitation from Fe ions in the environment. Instead, only the Fe-rich amorphous oxide on the top of inner oxide layer is defined as the outer oxide layer. This layer has not been reported before as such, which might be because the exposure time used in the literature (less than 1000 h) was not long enough or the results in literature lacked the resolution [1–10,18,19,21–26].

4.1.4. Outer oxide particles

Outer oxide particles have been often reported [1–10,18,19,21–26]. Since there was no orientation relationship between the oxide particles and the matrix (see Fig. 4), the formation of the oxide particles was considered to be mostly the result of precipitation from Cr, Fe and Ni ions in solution. As shown in Figs. 3d and 5, these oxide particles can be formulated as $(Fe,Cr,Ni)_3O_4$. Those on the sample surface directly exposed to the environment contain Ni 2+ and Fe 2+ in the M1 site and Cr 3+ and Fe 3+ in the M2 site (See Figs. 9 and 10). The particles in the crack flank appear to be pure magnetite ($FeFe_2O_4$) and those near the crack tip match with chromite ($FeCr_2O_4$). Although they are generally believed to provide no protection to the matrix, they appeared to be able to prevent the dissolution of the outer oxide layer (see Figs. 2 and 5) and the ingression of ions from the environment into the inner oxides. According to the results shown in Fig. 5a, the oxidation depth (not including the penetrative oxidation layer) under the outer oxide particles was smaller than the region without outer surface oxide particles. In addition, according to a recent work conducted by Dohr et al. [17], the initiation of SCC cracks could be delayed once the outer oxide particles form a continuous layer, since a higher stress is required to fracture the intergranular oxides.

4.2. Current understanding of surface oxidation mechanism

Based on the experimental evidence found in this study and the results discussed above, a detailed description of the surface oxidation of 316 L SS exposed to simulated PWR primary water is proposed, as shown in Fig. 11. Fig. 11a shows the initial stage of a cold-worked 316 L SS coupon exposed to PWR primary water. Once the specimen is exposed to the PWR primary water, oxidation starts to occur along the fast-diffusion channels (possibly dislocation channels) introduced by sample polishing and/or prior cold-work, as shown in Fig. 11b. Due to the high oxygen affinity, Cr is firstly oxidized by the inward diffusion of O while Fe diffuses out because of its higher diffusion rate. The oxides in the penetrative oxidation layer mainly consist of Cr_2O_3 and they are epitaxial with the matrix. Since Ni is nobler in this environment than Cr and Fe, and exhibits lower diffusion rate, it is “expelled” from the oxide into the neighboring matrix (occupying the vacancies left by the Fe and Cr). Meanwhile, Fe-rich oxide particles, that can incorporate cations from the environment, start to precipitate on the outer surface with no epitaxial relationship with the matrix. The size of the outer surface oxide particles increases with the exposure time and the surface oxidation develops into a deeper region, forming a continuous Cr-rich inner oxide layer, which will end up replacing the initial chromia nodules. The chromite oxides in the inner oxide layer are epitaxial with the matrix. As shown in Fig. 11c, oxidation is not completely prevented by the Cr-rich inner oxide layer, and the penetrative oxidation layer further develops ahead of the Cr-rich inner oxide layer. A part of Ni in the Cr-rich inner oxide layer is “expelled” into the penetrative oxidation layer (again, occupying the vacancies left by the Fe which started diffusing towards the environment), resulting in a local enrichment. Meanwhile, most of Fe and Ni in the Cr-rich inner layer diffuse out into the environment and then precipitate on the surface, forming the outer oxide particles. With the increase of the thickness of the inner oxide layer, outward diffusion of metallic elements and the inward diffusion of O becomes harder. As a result, oxidation slows down. After a long

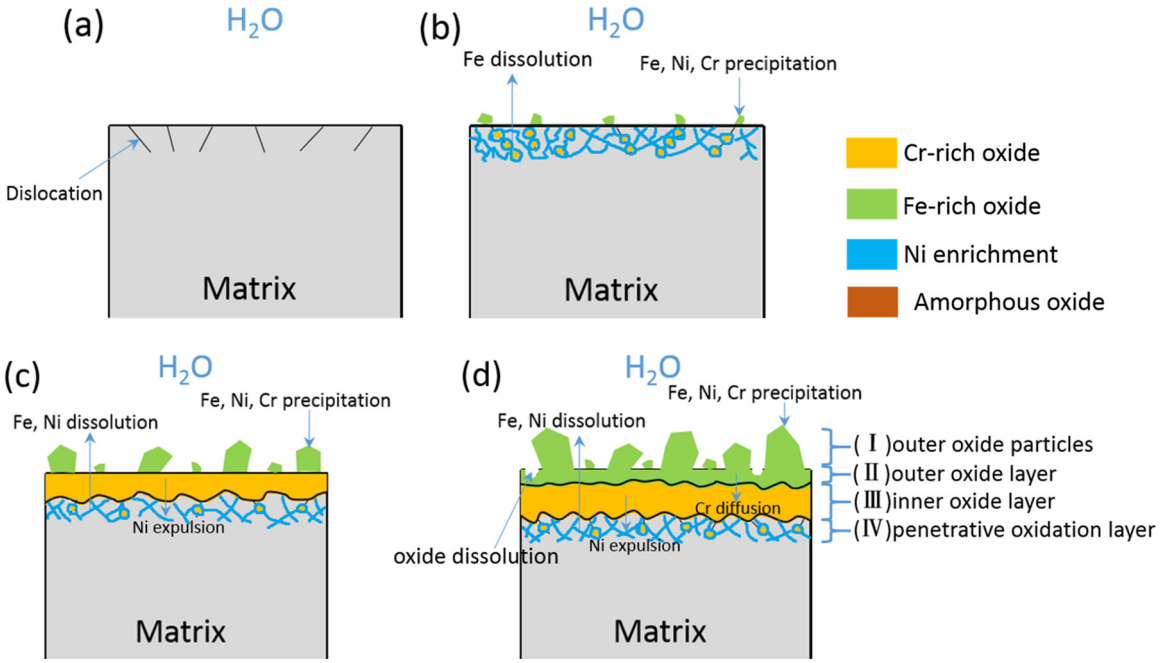

Fig. 11. Schematics of surface oxidation process of 316 L SS exposed to simulated PWR primary water at 340 °C.

enough exposure, the dissolution of Cr from the inner oxide layer into the environment leads to a Cr-depleted upper part, which eventually turns amorphous and has been referred to as the outer oxide layer. This new layer is not stable and starts to dissolve in the high temperature water. At some point, it loses its protective nature and oxidation starts to propagate deeper into the matrix, as shown in Fig. 11d.

4.3. Similarities and differences between surface, crack flank and crack tip oxidation

In order to compare the similarities and differences between the three regions, it is necessary to address their different exposure times. Since the 316 L SS coupon has been exposed to simulated PWR primary water for 2000 h, the exposure time for the surface oxide can be assumed to be the same. The crack flank oxide examined in Fig. 6, on the other hand, was around 1 μm away from a potentially active crack tip and should have experienced a shorter exposure. Using the measured CGR (6.21×10^{-8} mm/s), the time needed for the crack to propagate from the region of crack flank oxide (see Fig. 6) to the crack tip ahead (1 μm away) should be around 4.5 h. Bearing in mind that IOZ was always observed ahead of crack tips, averaging 300 nm, once can assume that 1.5 h (calculated based on the CGR) could have passed since the crack tip was exposed to the environment. This would give a maximum exposure time for the crack flank oxide shown in Fig. 6 of around 6 h. The depths and estimated exposure times of the surface oxide, crack flank oxide, and crack tip oxide are summarized in Table 6.

The results in Table 6 highlight the differences in oxidation kinetics in the three regions. The explanation is likely to be related to the differences in microstructure, applied stress, and, potentially, water chemistry. The first two are obvious. The microstructure ahead of the crack tip is a grain boundary with high defect density by nature, as opposed to the "matrix" nature of the crack flank and the sample surface. The applied stress is non-existent on the sample surface or very low if we consider residual stresses from prior cold-work and surface polishing. The applied stress on the crack flank will be high when next to the crack tip and gradually decreasing as this propagates further away. This has been proven to enhance oxidation [11,13,41–44]. Finally, the applied stress will be considerable at a crack tip, particularly if it has become the dominant one, as assumed for the one chosen in this study. Regarding the water chemistry, if it was the same inside and outside the SCC crack [5], the morphology and chemical composition of the crack flank and tip oxides should be similar to those on the surface. We found substantial similarities and some differences (see Figs. 6 and 10c and Tables 2 and 3). The structure of the layers is similar, although no clear amorphous outer oxide was found on the crack flank. Composition-wise, Fe and Cr from the environment clearly incorporate into the outer oxide particles and partly into the outer (Fe) and inner (Cr) oxide layer on the sample surface, but not in those on the crack flank or tip. The absence of an amorphous outer oxide layer and outer surface particles in the crack tip oxide can be due to its much shorter exposure time.

The selective oxidation-induced Ni-rich zone was also observed in the penetrative oxidation layer of the surface oxide and the crack flank oxide (see Figs. 5b and 6 b). Atomic-resolution images proved that the Ni-rich region had the same orientation with the surrounding matrix, indicating that the rejected Ni from selective oxidation adopted the same lattice as the hosting grain, which was similar to the Ni-rich zone (grain boundary migration zone) ahead of the crack tips. However, the redistribution of Ni in the penetrative oxidation layer proceeded along dislocations and had no preferred destination, while the redistribution of Ni at the grain boundary tends to prefer one grain orientation, leading to the formation of grain boundary migration. The underlying

Table 6
Summary of the depths and estimated exposure times of the surface oxide, crack flank oxide, and crack tip oxide.

Oxides	Depths (nm)	Estimated exposure times (h)
Surface oxide	50˜120 (exclude outer surface oxide particles)	2000
Crack flank oxide	50˜100 (exclude crack flank oxide particles)	˜6
Crack tip oxide	240˜320 (along the grain boundary direction)	˜1.5

reasons contributing to this difference is still unclear, which might be due the content of defects in one grain was much higher than in the other grain (prior cold-work lead to preferential deformation in one grain).

4.4. Implication for SCC

Based on the results shown in this study and the discussion above, the mechanisms controlling the surface oxidation, crack flank oxidation, and the crack tip oxidation are proposed to be similar. However, cation availability and stress condition are clearly different. As explained in our previous works [11,13,24,41] and based on the work of Dohr et al. [17], the authors consider that the grain boundary oxidation is a prerequisite for SCC to occur and the factors that can affect oxidation also affect SCC crack growth.

SCC has been reported in many austenitic alloys after exposure to the PWR primary water [11–16]. Although many phenomena can affect primary water SCC, the controlling mechanism is still unresolved. Several models have been proposed to explain the mechanisms of SCC, including film rupture, hydrogen embrittlement, and intergranular selective oxidation [45–50]. The intergranular selective oxidation model, which was first introduced by Scott et al. [46] and discussed by [11–15], assumes solid state diffusion of oxygen down grain boundaries, which are preferentially oxidized once exposed to PWR primary water, causing the oxidized grain boundaries to crack more easily because of grain boundary embrittlement. The brittle nature of the oxidized grain boundary has been experimentally proven by many researchers through direct measurement of the mechanical strength of oxidized and unoxidized grain boundaries [17,51,52]. Since intergranular selective oxidation was also observed ahead of the crack tip in the current study (see Fig. 8), the SCC mechanism can also be described as selective intergranular oxidation.

According to the recent work by Bruemmer et al. [12] and Shen et al. [13], selective oxidation of the grain boundary could inject vacancies into the intergranular oxide, leading to the formation of a porous intergranular oxide. The porous intergranular oxide cannot protect the grain boundary efficiently, which will enhance the intergranular oxidation and then accelerate SCC crack growth. The formation of porous intergranular oxide was believed to be the result of selective oxidation under a certain environment [12–14,16,36,40]. Since the content of dissolved hydrogen used in the current study located at the equilibrium of Ni/NiO, Cr and Fe were readily oxidized while the oxidation of Ni was minimum, especially in the inner region of the oxide, where the corrosion potential is expected to be lower. For this reason, the oxidation occurred in the grain boundary ahead of the crack tip was selective (see Fig. 9c). The oxidation-induced porous intergranular oxide might be able to explain the enhanced intergranular oxidation ahead of the crack tip examined in the current study.

Recently, grain boundary migration has been frequently reported in Alloy 600 and Alloy 690 after exposed to simulated PWR primary water or high-temperature H_2-steam. Grain boundary migration was also observed in the current study, which was believed to be caused by the selective oxidation of solute elements (Cr and Fe) [12,13,16,33–38,45]. According to the recent works conducted by Bertali et al. [34,35], once grain boundary migration occurred, the intergranular oxidation would be enhanced in two ways. The first one is that the chemical composition alteration in the migrated region could lead to local volume change and the volume change could then introduce tensile or compressive stress in the migrated region, which would fracture the intergranular oxide and decrease its protectiveness. The second one is that Cr was depleted in the migrated grain boundary (see Fig. 8) and protective oxide was difficult to form, resulting in faster intergranular oxidation.

The formation of a Ni-rich zone (around the penetrative oxidation layer) was also observed in the surface oxide and the crack flank oxide. Since both the formation of the grain boundary migration ahead of the crack tip and the Ni-rich zone in the surface oxide were caused by the selective oxidation, once the Ni-rich zone was observed in the surface oxide, the occurrence of porous intergranular oxide and grain boundary migration ahead of the crack tip could be expected. According to the discussion above, both porous intergranular oxide and grain boundary migration ahead of the crack tip were detrimental to SCC.

5. Conclusions

The surface, crack flank and crack tip oxidation have been characterized by high-resolution ATEM. The results are compared and the related oxidation mechanisms are proposed. The implications to SCC are discussed. The main findings are summarized as follows:

1 After 2000 h of exposure, the oxide film formed on 316 L SS has a triplex structure, a Cr-rich penetrative oxidation layer, a Cr-rich inner oxide layer, and a Fe-rich outer oxide layer. A further outer incomplete layer exists, made of Fe-rich discrete oxide particles.
2 The penetrative oxidation layer is formed by the selective oxidation of Cr along the fast-diffusion channels. The formation of inner oxide layer is dominated by the solid-state growth mechanism. The inner layer oxide is Cr-rich spinel and epitaxial to the matrix while the outer layer oxide is amorphous and dissolves into the solution eventually. The formation of the outer surface oxide particles is the result of precipitation of corrosion products and they have no crystallographic orientation relationship with the matrix.
3 The electrochemical potential in the crack is supposed to be similar to that on the sample surface because the microstructure and chemistry of the crack flank oxides are similar to those on the surface. A similar oxidation mechanisms is suggested for both cases, although the water chemistry is different, with a higher concentration of dissolved cations in the open environment causing the precipitation of Fe-rich spinel containing Cr and Ni instead of magnetite. In addition, crack flank oxidation is faster than on the free surface because of the applied-stress.
4 Intergranular selective oxidation develops ahead of the crack tip at a rate over 3 orders of magnitude faster than that at the surface. The enhanced intergranular oxidation rate is supposed to be cause by the higher dislocation density and applied-stress and further contributed by the formation of porous intergranular oxide and grain boundary migration.

Acknowledgements

This work is supported by National Science and Technology Major Project of China, No. 2011ZX06004. Zhao Shen is grateful to China Scholarship Council for providing financial support. The EPSRC (EP/K040375/1, EP/N010868/1 and EP/R009392/1) grants are also acknowledged for funding this research.

Appendix A. Supplementary data

Supplementary material related to this article can be found, in the online version, at doi:https://doi.org/10.1016/j.corsci.2018.12.020.

References

[1] B. Stellwag, The mechanism of oxide film formation on austenitic stainless steels in high temperature water, Corros. Sci. 40 (1998) 337–370.
[2] R. Soulas, M. Cheynet, E. Rauch, T. Neisius, L. Legras, C. Domain, Y. Brechet, TEM investigations of the oxide layers formed on a 316L alloy in simulated PWR environment, J. Mater. Sci. 48 (2013) 2861–2871.
[3] G. Han, Z. Lu, X. Ru, J. Chen, J. Zhang, T. Shoji, Properties of oxide films formed on 316L SS and model alloys with modified Ni, Cr and Si contents in high temperature water, Corros. Sci. 106 (2016) 157–171.
[4] T. Terachi, K. Fujii, K. Arioka, Microstructural characterization of SCC crack tip and oxide film for SUS 316 stainless steel in simulated PWR primary water at 320 C, J. Nucl. Sci. Technol. 42 (2005) 225–232.
[5] M. Vankeerberghen, G. Weyns, S. Gavrilov, J. Henshaw, J. Deconinck, The

electrochemistry in 316SS crevices exposed to PWR-relevant conditions, J. Nucl. Mater. 385 (2009) 517–526.
[6] Y. Han, J. Mei, Q. Peng, E.H. Han, W. Ke, Effect of electropolishing on corrosion of nuclear grade 316L stainless steel in deaerated high temperature water, Corros. Sci. 112 (2016) 625–634.
[7] D.H. Lister, R.D. Davidson, E. McAlpine, The mechanism and kinetics of corrosion product release from stainless steel in lithiated high temperature water, Corros. Sci. 27 (1987) 113–140.
[8] S.E. Ziemniak, M. Hanson, Corrosion behavior of 304 stainless steel in high temperature, hydrogenated water, Corros. Sci. 44 (2002) 2209–2230.
[9] S. Lozano-Perez, D.W. Saxey, T. Yamada, T. Terachi, Atom-probe tomography characterization of the oxidation of stainless steel, Scr. Mater. 62 (2010) 855–858.
[10] A. Turnbull, K. Mingard, J.D. Lord, B. Roebuck, D.R. Tice, K.J. Mottershead, N.D. Fairweather, A.K. Bradbury, Sensitivity of stress corrosion cracking of stainless steel to surface machining and grinding procedure, Corros. Sci. 53 (2011) 3398–3415.
[11] M. Meisnar, M. Moody, S. Lozano-Perez, Atom probe tomography of stress corrosion crack tips in SUS316 stainless steels, Corros. Sci. 98 (2015) 661–671.
[12] S.M. Bruemmer, M.J. Olszta, M.B. Toloczko, D.K. Schreiber, Grain boundary selective oxidation and intergranular stress corrosion crack growth of high-purity nickel binary alloys in high-temperature hydrogenated water, Corros. Sci. 131 (2018) 310–323.
[13] Z. Shen, K. Arioka, S. Lozano-Perez, A mechanistic study of SCC in Alloy 600 through high-resolution characterization, Corros. Sci. 132 (2018) 244–259.
[14] M. Sennour, P. Laghoutaris, C. Guerre, R. Molins, Advanced TEM characterization of stress corrosion cracking of Alloy 600 in pressurized water reactor primary water environment, J. Nucl. Mater. 393 (2009) 254–266.
[15] Y.S. Lim, H.P. Kim, S.S. Hwang, Microstructural characterization on intergranular stress corrosion cracking of Alloy 600 in PWR primary water environment, J. Nucl. Mater. 440 (2013) 46–54.
[16] W. Kuang, M. Song, G.S. Was, Insights into the stress corrosion cracking of solution annealed alloy 690 in simulated pressurized water reactor primary water under dynamic straining, Acta Mater. 151 (2018) 321–333.
[17] J. Dohr, D.E. Armstrong, E. Tarleton, T. Couvant, S. Lozano-Perez, The influence of surface oxides on the mechanical response of oxidized grain boundaries, Thin Solid Films 632 (2017) 17–22.
[18] S. Wang, Y. Hu, K. Fang, W. Zhang, X. Wang, Effect of surface machining on the corrosion behaviour of 316 austenitic stainless steel in simulated PWR water, Corros. Sci. 126 (2017) 104–120.
[19] Y.Z. Huang, J.M. Titchmarsh, TEM investigation of intergranular stress corrosion cracking for 316 stainless steel in PWR environment, Acta Mater. 54 (2006) 635–641.
[20] P.L. Andresen, J. Hickling, A. Ahluwalia, J. Wilson, Effects of hydrogen on stress corrosion crack growth rate of nickel alloys in high-temperature water, Corrosion 64 (2008) 707–720.
[21] S. Cissé, L. Laffont, B. Tanguy, M.C. Lafont, E. Andrieu, Effect of surface preparation on the corrosion of austenitic stainless steel 304L in high temperature steam and simulated PWR primary water, Corros. Sci. 56 (2012) 209–216.
[22] W. Kuang, X. Wu, E.H. Han, The oxidation behaviour of 304 stainless steel in oxygenated high temperature water, Corros. Sci. 52 (2010) 4081–4087.
[23] R.P. Matthews, R.D. Knusten, J.E. Westraadt, T. Couvant, Intergranular oxidation of 316L stainless steel in the PWR primary water environment, Corros. Sci. 125 (2017) 175–183.
[24] K. Kruska, S. Lozano-Perez, D.W. Saxey, T. Terachi, T. Yamada, G.D. Smith, Nanoscale characterisation of grain boundary oxidation in cold-worked stainless steels, Corros. Sci. 63 (2012) 225–233.
[25] D.K. Schreiber, M.J. Olszta, D.W. Saxey, K. Kruska, K.L. Moore, S. Lozano-Perez, S.M. Bruemmer, Examinations of oxidation and sulfidation of grain boundaries in alloy 600 exposed to simulated pressurized water reactor primary water, Microsc. Microanal. 19 (2013) 676–687.
[26] J. Chen, Q. Xiao, Z. Lu, X. Ru, H. Peng, Q. Xiong, H. Li, Characterization of interfacial reactions and oxide films on 316L stainless steel in various simulated PWR primary water environments, J. Nucl. Mater. 489 (2017) 137–149.
[27] J. Robertson, The mechanism of high temperature aqueous corrosion of stainless steels, Corros. Sci. 32 (4) (1991) 443–465.
[28] R. Winkler, Studies on anticorrosion layers on steels typical for power stations, Kernenergie 32 (1989) 188–193.
[29] S. Lozano-Perez, A guide on FIB preparation of samples containing stress corrosion crack tips for TEM and atom-probe analysis, Micron 39 (2008) 320–328.
[30] F. de la Peña, M.-H. Berger, J.-F. Hochepied, F. Dynys, O. Stephan, M. Walls, Mapping titanium and tin oxide phases using EELS: an application of independent component analysis, Ultramicroscopy 111 (2011) 169–176.
[31] T.L. Daulton, B.J. Little, Determination of chromium valence over the range Cr (0)–Cr (VI) by electron energy loss spectroscopy, Ultramicroscopy 106 (2006) 561–573.
[32] C. Colliex, T. Manoubi, C. Ortiz, Electron-energy-loss-spectroscopy near-edge fine structures in the iron-oxygen system, Phys. Rev. B 44 (1991) 11402.
[33] B. Langelier, S.Y. Persaud, A. Korinek, T. Casagrande, R.C. Newman, G.A. Botton, Effects of boundary migration and pinning particles on intergranular oxidation revealed by 2D and 3D analytical electron microscopy, Acta Mater. 131 (2017) 280–295.
[34] G. Bertali, F. Scenini, M.G. Burke, Advanced microstructural characterization of the intergranular oxidation of Alloy 600, Corros. Sci. 100 (2015) 474–483.
[35] G. Bertali, F. Scenini, M.G. Burke, The effect of residual stress on the preferential intergranular oxidation of alloy 600, Corros. Sci. 111 (2016) 494–507.
[36] S.Y. Persaud, A. Korinek, J. Huang, G.A. Botton, R.C. Newman, Internal oxidation of Alloy 600 exposed to hydrogenated steam and the beneficial effects of thermal treatment, Corros. Sci. 86 (2014) 108–122.
[37] S.Y. Persaud, S. Ramamurthy, R.C. Newman, Internal oxidation of alloy 690 in hydrogenated steam, Corros. Sci. 90 (2015) 606–613.
[38] S.Y. Persaud, B. Langelier, A. Korinek, S. Ramamurthy, G.A. Botton, R.C. Newman, Characterization of initial intergranular oxidation processes in alloy 600 at a sub-nanometer scale, Corros. Sci. 133 (2018) 36–47.
[39] R. Dieckmann, Point defects and transport properties of binary and ternary oxides, Solid State Ion. 12 (1984) 1–22.
[40] B. Langelier, S.Y. Persaud, R.C. Newman, G.A. Botton, An atom probe tomography study of internal oxidation processes in Alloy 600, Acta Mater. 109 (2016) 55–68.
[41] S. Lozano-Perez, T. Yamada, T. Terachi, M. Schröder, C.A. English, G.D.W. Smith, C.R.M. Grovenor, B.L. Eyre, Multi-scale characterization of stress corrosion cracking of cold-worked stainless steels and the influence of Cr content, Acta Mater. 57 (2009) 5361–5381.
[42] Z. Lu, T. Shoji, S. Yamazaki, K. Ogawa, Characterization of microstructure, localized deformation and microchemistry in Alloy 600 heat-affected zone and stress corrosion cracking in high temperature water, Corros. Sci. 58 (2012) 211–228.
[43] S. Lozano-Perez, K. Kruska, I. Iyengar, T. Terachi, T. Yamada, The role of cold work and applied stress on surface oxidation of 304 stainless steel, Corros. Sci. 56 (2012) 78–85.
[44] T. Terachi, T. Yamada, T. Miyamoto, K. Arioka, SCC growth behaviors of austenitic stainless steels in simulated PWR primary water, J. Nucl. Mater. 426 (2012) 59–70.
[45] M.G. Burke, G. Bertali, E. Prestat, F. Scenini, S.J. Haigh, The application of in situ analytical transmission electron microscopy to the study of preferential intergranular oxidation in alloy 600, Ultramicroscopy 176 (2017) 46–51.
[46] P.M. Scott, M. Le Calvar, Some possible mechanisms of intergranular stress corrosion cracking of alloy 600 in PWR primary water, Proceedings of the Sixth International Symposium on Environmental Degradation of Materials in Nuclear Power Systems-Water Reactors, (TMS), (1993), pp. 657–665.
[47] H.K. Birnbaum, P. Sofronis, Hydrogen-enhanced localized plasticity—a mechanism for hydrogen-related fracture, Mater. Sci. Eng. A 176 (1994) 191–202.
[48] F.P. Ford, Quantitative prediction of environmentally assisted cracking, Corrosion 52 (1996) 375–395.
[49] T. Magnin, A. Chambreuil, B. Bayle, The corrosion-enhanced plasticity model for stress corrosion cracking in ductile fcc alloys, Acta Mater. 44 (1996) 1457–1470.
[50] K. Arioka, WR Whitney Award Lecture: change in bonding strength at grain boundaries before long-term SCC initiation, Corrosion 71 (2014) 403–419.
[51] H. Dugdale, D.E. Armstrong, E. Tarleton, S.G. Roberts, S. Lozano-Perez, How oxidized grain boundaries fail, Acta Mater. 61 (2013) 4707–4713.
[52] K. Fujii, T. Miura, H. Nishioka, K. Fukuya, Degradation of grain boundary strength by oxidation in alloy 600, Mater. Trans. 52 (2011) 1447–1458.